ORIGINAL ARTICLE

Groove configurations of a flux-cored arc welding process used in critical structures of precision mechanical presses—mechanical and metallurgical studies

Kuo-Hsia Ling · Yiin-Kuen Fuh · Kun-Ling Wu · Tin-Chun Kuo · Chung-Yu Huang

Abstract This paper utilized a flux-cored arc welding (FCAW) technique and investigated various groove configurations as well as multi-pass welding sequences to create welding specifications in the precision mechanical press industry. Experimental investigations were conducted to examine the influence of three different groove configurations of 40-mm-thick JIS SS400 structural steel welded joints on mechanical and metallurgical properties. Mechanical properties of the welded joints were evaluated by uniaxial tensile testing and Charpy V-notch (CVN) impact testing at room temperature. Simultaneously after a multi-pass welding sequence, various degrees of thermal treatments such as tempering or normalization inevitably occur in the heat-affected zone (HAZ). The unfavorable microstructures in the HAZ and reheated zones can be intentionally modified via the above procedure such that the toughness and microhardness of the HAZ improve. The experimental results revealed that of the three types of groove configurations (C1, C, and F), groove type C1 possessed the maximum yield strength (YS) and ultimate tensile strength (UTS) while groove type F possessed the highest CVN values tested at room temperature. The fundamental reason may be attributed to heat dissipation characteristics of each groove configuration and associated exertion of the multi-pass welding sequence. Microstructural and morphological features as revealed through an optical microscope also indicate a significant influential factor of these joints among the different groove configurations. Therefore, grain refinement of varying degrees can be obtained due to the variation of thermal characteristics of heat input/dissipation; thus, various mechanical and CVN impact properties can be obtained.

Keywords Groove configurations · Flux-cored arc welding · Precision mechanical press · Metallurgy · Multi-pass welding

K.-H. Ling · Y.-K. Fuh (✉) · C.-Y. Huang
Department of Mechanical Engineering, National Central University, No. 300, Jhongda Rd., Jhongli City, Taoyuan County 32001, Taiwan
e-mail: mikefuh@ncu.edu.tw

K.-H. Ling · T.-C. Kuo
Shieh Yih Machinery Industry Co., Ltd., No. 446, Nan Shang Rd., Kueishan Village, Taoyuan County 33392, Taiwan

K.-L. Wu
Department of Mechanical Engineering, Tungnan University, No. 152, Section 3, Beishen Rd., Shenkeng District New Taipei City 22202, Taiwan

1 Introduction

Welding is widely facilitated in industries ranging from construction, shipbuilding, automobile manufacturing, and machinery due to the highly favorable properties of reliable and efficient metal-joining techniques [1]. A widely adopted method in welding is flux-cored arc welding (FCAW), where the coalescence between the welding metal (WM) and the base metal (BM) can be achieved by continuously feeding welding wire in a semi-automatic or automatic fashion [2, 3]. An improved variant which includes both externally supplied shielding gas and flux-generated liquid slag is referred to as gas-shielded flux-cored arc welding (FCAW-G) and is commonly used for construction due to high welding speed (productivity) and compact equipment (portability). Furthermore, FCAW-G improves the restriction of the stick electrodes in shielded metal arc welding (SMAW) and also simultaneously possesses the advantage of gas metal arc welding (GMAW) and submerged arc welding (SAW) processes [4].

The most important welding parameters are highly associated with heat inputs such as current, voltage, average travel speed, and shielding gas flow rate. Furthermore, the heat relevant effect (such as arc power or welding energy and

derivatives of effective heat input) will inevitably have a direct impact on the bead geometry, microstructure, and mechanical properties of low alloy steels [5, 6]. Several different compositions of shielding gas with flux-cored wires were investigated previously, and important weld quality factors such as spatter rates, chemical compositions, and mechanical tests have been systematically reported [7]. In addition, the proper selection of shielding gas greatly improves the arc plasma and related current path as well as the transfer of thermal energy on the pool. The two most common types of shielding gas are 100 % carbon dioxide (CO_2) and 75–85 % argon (Ar)/balance CO_2. For the welding of irons and steels, CO_2 is the preferred choice due to the lower ionization potential for easier initiation of an arc and a higher thermal conductivity level [8]. The penetration and bead width were also found to be closely related to welding parameters, while the main driving force is the heat input [9].

Many different groove designs are prevalently used for structures in typical pressure vessels and ship building such as the traditional V, butt, and U grooves [10]. Previous studies revealed that different groove formations predominately dictate mechanical properties such as maximum yield strength (YS) and ultimate tensile strength (UTS) [11]. Another important parameter is welding bead number, instead of welding sequences, and was previously proven such that the improvement on microstructure as well as reduction in the microhardness was achieved [12]. The loss of hardness and strength in the welded heat-affected zone (HAZ) due to heat thermal cycles and the effect of groove design on mechanical and metallurgical properties of quenched and tempered welding joints were extensively investigated in previous experiments [13, 14]. Furthermore, based on a continuous cooling transformation (CCT) diagram of a low carbon steel welded joint, formation of a combination of ferrites in the grain boundary/sideplate/acicular was observed. Further, bainite (B) and martensite (M) structures are found to be heavily dependent on the heat input and cooling rate, and this kind of microstructure is the commonly found microstructure in the WM zone. Meanwhile, the strength of a welding joint can be improved by a faster cooling rate [15]. However, fracture was also reported to be highly attached to the mismatch of yield strengths between a BM and a WM after the joining process [16]. For the impact toughness, previous studies suggested that a high heat input will induce coarse grains in the HAZ, which results in decreased hardness and increased toughness in low carbon steel [17, 18]. The increased volume fraction of acicular ferrite (ACF) was also experimentally correlated to a substantial improvement of the impact property [19]. On the other hand, the adversely formed martensite–austenite (M–A) constituent during welding

was considered detrimental and generally decreases the toughness of a welding joint [20]. In this paper, the influence of groove designs and welding sequence were extensively investigated, in particular, on the mechanical and metallurgical performance of the JIS SS400 structural steel plate. For welding 40-mm-thick steels with a butt joint configuration, three different groove configurations (C1, C, and F) were selected. Owing to the fact that a precision press cannot be mass produced due to versatile applications, all the frames were welded in the manual mode while the heat input per unit length of the weld for each joint was maintained at a variation of 250 J/mm. The mechanical properties of welding joints were evaluated through uniaxial tensile tests and Charpy V-notch (CVN) tests. Microhardness studies were performed across different zones of the welding joint in various groove geometries. Microstructures of the weld and the HAZ were investigated by optical microscopy. Finally, the fracture surfaces in these joints subjected to tensile and impact testing was assessed by scanning electron microscope (SEM) studies.

In the metal forming industry, the precision press is widely used for various components and in many sectors such as agriculture, automobile, 3C electronics (computer, communication, and consumer), and the military. The most critical and repaired structure is the press frame as illustrated in Fig. 1, which is a straight side mechanical press. This seemingly simple construction is in fact a geometrically complex structure made of a JIS SS400 structural steel plate of various dimensions. Among the construction of a press frame, the slide and crown are the two most critical components to production safety and fabricated through a FCAW-G process. In particular, according to the European CE mark, mechanical presses safety requirements (EN-692), the quality of welding joints should fully comply due to the extremely rigorous conditions during the manufacturing processes. Consequently, both slide and crown structures should be fully inspected via liquid penetrant testing, which is a non-destructive testing (NDT) method [21]. More importantly, these welded sliders with crown structures are constantly subjected to several repair welding operations during manufacture. Therefore, a strict compliance with the standards of the American Welding Society (AWS) during repair welding operations is compulsory to ensure the welding effects on the microstructure, mechanical properties, and structural integrity.

2 Experimental procedures

2.1 Material and welding procedure

The BM was made of a SS400 structural steel with a thickness of 40 mm. The WM used was a TWE-711 (Tien Tai Electrode

Fig. 1 **a** The optical photo of a commercial heavy duty precision press (SLG-1000) with a 1000 ton capacity. For the press frame, three types of welding grooves, namely C1, C, and F, were chosen and constructed by JIS SS400 structural steel. Groove types C1 and C are shown in the **b** crown while groove type F is shown in the **c** slider
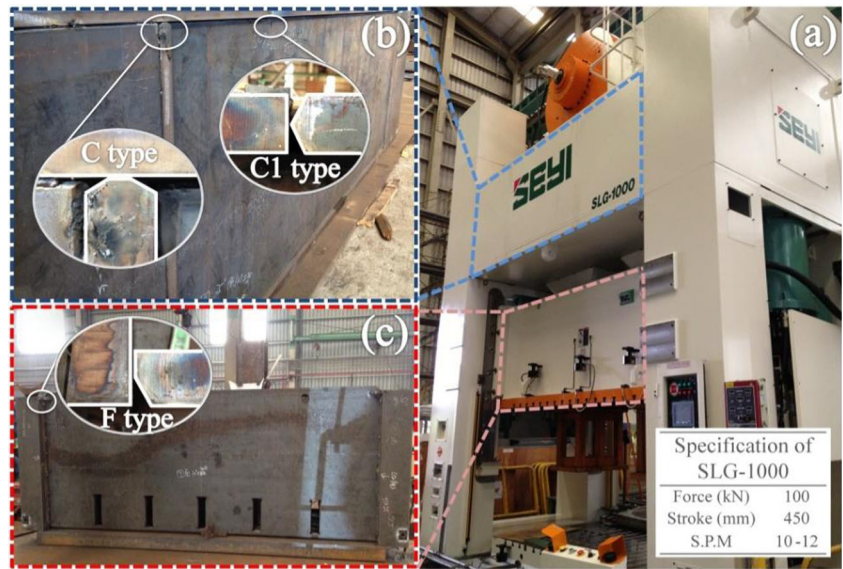
Co. Ltd) welding wire. The composition and mechanical properties of BM and welding wire are listed in Tables 1 and 2, respectively. FCAW-G with a multi-pass butt-welding joint type was applied. The welding parameters such as current, voltage, average travel speed, and shielding gas flow rate are listed in Table 3. The continuous welding with multi-pass, welding wires of 1.6 mm diameter was carried out with particular focus on the weld joint types and related mechanical properties such as tensile strength, microhardness, and impact toughness. A total of three joint types (C1, C, and F) and wires of 1.6 mm diameter were sequentially welded at a designated order while the welding current, voltage, travel speed, and inert gas flow were fixed.

2.2 Preparation of tensile and impact specimens

Figure 2 shows the schematic diagram of tensile and impact specimens machined from the weldments, which the beads of multi-pass welding is illustrated as the welding progress sequentially. Tensile tests were conducted using the BM made of JIS SS400 structural steel uniaxial tensile conditions and with the rolling direction of the plate coinciding with the tensile axis of the specimens. Tensile test specimens, each with an overall length of 300 mm, gage length of 120 mm, grip section length of 75 mm, fillet radius of 25 mm, width of 30 mm, grip section width of 40 mm, and thickness of 5 mm, were used to obtain the tensile properties of the FCAW-G welding joint as shown in Fig. 4. The dimensions of the Charpy impact specimens were prepared to evaluate the impact toughness of the

WM bead sequence and SS400 groove as shown in Fig. 3. All impact tests were carried out according to American Society for Testing and Materials (ASTM) E23 standards [22] (10 mm×55 mm with a 2-mm deep, 45° V-notch, and a 0.25-mm tip radius at the center of the specimen in the center of the weldment) and were used to prepare the in-plane specimens, and wire electrical discharge machining (WEDM) is capable of precisely sampling the specimens with repeatedly close tolerance, which coincides with the rolling direction of the plate. This research predominantly examines the groove configuration of welding, which immensely affects the tensile rupture strength, impact toughness, and microhardness. The details of various groove configurations are presented in Fig. 4.

2.3 Microstructural characterization

For the microstructural examination, the specimens were initially taken from the weld section and then ground with silicon carbide (SiC) paper in the order of sand paper number #240, #400, #600, #800, #1000, and #1500. Prior to an optical microscope (OM) examination, a fine 0.1 μm aluminum oxide (Al_2O_3) solution was used to produce a mirror-like polished surface with a surface roughness (Rmax) of 0.1 μm, subsequently etched with 3 % nital solution etchant, and ultrasonically cleaned by acetone. Moreover, the fracture surfaces of the WM specimens after tensile and Charpy impact tests were then examined via a SEM.

Table 1 Chemical composition and mechanical properties of the BM: SS400 structural steel

Base metal	% C	% Si	% Mn	% P	% S	% Fe	Yield strength (MPa)	Ultimate strength (MPa)	Elongation (%)
SS400	0.14	–	<1.06	<0.023	<0.05	Balance	300	400–510	32

Table 2 Chemical composition and mechanical properties of the welding wire: TWE-711

Welding wire	% C	% Si	% Mn	% P	% S	% Fe	Yield strength (MPa)	Ultimate strength (MPa)	Elongation (%)
TWE-711	0.05	0.05	1.45	0.015	0.008	Balance	530	580	29

2.4 Mechanical testing

Tensile test specimens were sectioned from the weldment (perpendicular to the welding direction). Tensile tests were carried out using a commercial closed-loop servo-hydraulic test machine, MTS-810, operating at a constant speed of 2 mm/min. In compliance with the ASTM E23 standards, the CVN impact test was conducted on the welds at room temperature, as shown in Fig. 3. In order to characterize the mechanical properties of the welds, the test specimens were machined perpendicular to the welding direction such that the notch was located in the center of the WM. The microhardness profiles were measured to identify various regions of interests such as the WM, HAZ, and BM via Vickers microhardness measurements across the welds, at a load of 1000 g and a dwell time of 15 s according to ASTM E384 [23].

2.5 Welding groove configurations

As shown schematically in Fig. 4 a1–a3, three different groove configurations were machined from the SS400 BM. Prior to welding, the plates were thoroughly cleaned and firmly clamped onto a fixture. A total of five to 14 weld passes were sequentially welded, i.e., corresponding to C1, C, and F groove configurations. In Fig. 4 b1–b3, a FCAW-G process was employed for the multi-pass welding (four to 12 weld passes) on the root and one to two main weld passes. This present case of average heat input was calculated to be in the range 2.15–2.4 kJ/mm using a welding wire of 1.6 mm diameter. The mechanical properties such as impact toughness, tensile strength, and microhardness for SS400 structural steel of the three types of weld grooves (C1, C, and F) were evaluated systematically.

3 Results and discussion

### 3.1 Metallographic studies

3.1.1 Macrostructure

The metallographic studies of the weld cross sections for the three types welding joints C1, C, and F are presented in Fig. 4 c1–c3. As illustrated by the numbers 1, 2, and 3 which denote the WM, HAZ, and BM, respectively, different zones of the welding joints can be clearly identified. From the weld cross sections, all three welding joints C1, C, and F show observable subsurface (interface) defects due to insufficient melting. These defects are unavoidable in the press frame industry due to restrictions on weld structures. The impact of these defects on mechanical properties is the main focus of this paper. Furthermore, variations in groove configurations, welding sequences, and the number of welds along with their associated heat dissipation characteristics have a decisive role in the mechanical and metallurgical properties of these welded structures.

3.1.2 The effect of sequence deposition on the microstructure

Figure 5 presents distinctively different microstructures in a single bead weld. Features of columnar and fine-grained microstructures between the WM and HAZ as well as a clear boundary between the BM and WM can be easily identified [12].

Several distinctive regions such as the WM, HAZ, and BM can be clearly identified as shown in Fig. 6a–c, respectively. From the optical micrograph, various microstructures such as Widmanstatten ferrite (WF), ACF, pearlite (P) ferrite (F), and M can be identified as indicated in previous study [24]. There is approximately 34 % of P (denoted by red), 61 % of F (denoted by green), and 5 % of M (denoted by yellow) in the WM as calculated in Fig. 6 a1–a2 (using image analyzing

Table 3 Welding parameters of FCAW-G

No.	Groove	Diameter of welding wire	Current (A)	Voltage (V)	Average travel speed (mms^{-1})	Shielding gas flow rate (CO_2) (L min^{-1})
1	C1	1.6	400	28–30	5.0–5.2	20
2	C	1.6	400	28–30	5.0–5.2	20
3	F	1.6	400	28–30	5.0–5.2	20

Fig. 2 Schematic diagram of tensile and impact specimens machined using the weldments
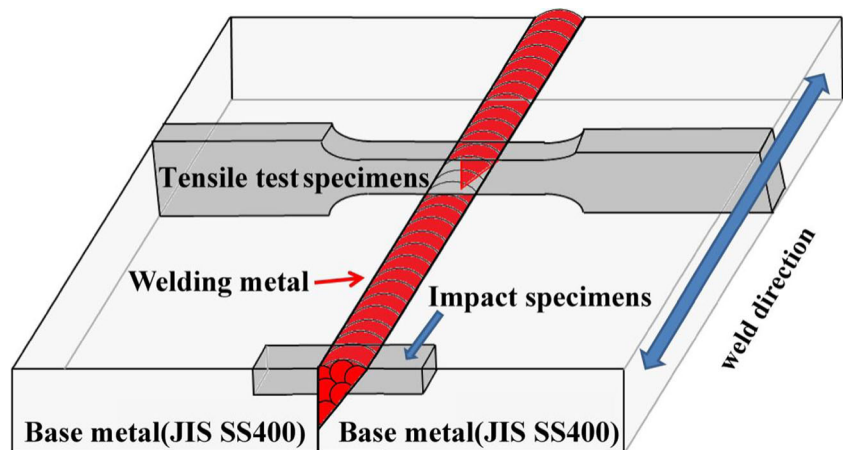
software, Image Pro Plus [25]. Note that the phase percentage of ferrite, F, also includes WF and ACF. In comparison, the HAZ microstructure in Fig. 6 b1–b2 reveals the grain-coarsening region and grain-refining region with the existence of WF, P, ferrite grains, and M [3, 24]. Calculations revealed that there is approximately 41 % of P, 48 % of F, and 11 % of M in the HAZ region. On the other hand, the BM microstructure in Fig. 6 c1–c2 primarily shows two phases of F and P with an area fraction of approximately 84 and 16 %, respectively. Furthermore, it was experimentally found that with increasing heat input, small amounts of grain boundary allotriomorphic microstructure and/or WF can be identified and this agrees well with a previous study on high strength low alloy (HSLA) steels by pulsed gas metal arc welding [15].

3.2 Mechanical properties

3.2.1 Tensile properties

As shown in Fig. 7, for uniaxial tensile testing of all three types of joints, it is observed that all fractures occurred in the HAZ, suggesting that preferential plastic deformation existed in the HAZ for all the joints. The calculated mismatch of yield strength between the BM and WM is more than 15 % as stated in Tables 1 and 2, which is in agreement with the observed failures in the HAZ. A previously reported experiment also confirmed that a strength mismatch of more than 15 % will

inevitably induce plastic flow and reduce strength and ductility of the joint, especially in the weakest zone [26].

As expected, tensile fracture occurred in the WM of all the joints. It is further seen that a mismatch factor (M) [16] (defined as the ratio of YS of the WM to the BM-(WMYS/BMYS)) for all the joints lies between 1.15 and 1.20, which suggests that plastic deformation may be highly localized in the HAZ. As a comparison, previously reported M values range from 0.40 to 0.50, which tends to make plastic deformation highly localized in the WM [11]. In addition, a significant softening due to welding arc heat and a resultant tempering effect is observed in the HAZ of these joints. The vulnerability of the HAZ can be further compared with the unaffected WM such that the variation of M values is mainly attributed to the heat dissipation characteristics of various groove configuration. Therefore, as stress was applied, the crack initiated at the central region of the HAZ for the C1 and C joints, while that of the F joint initiated at the top pass region of the HAZ. This could mainly be due to stress concentration of different groove configurations. Therefore, the crack propagation continues to the rest of the weld pass region as illustrated in Fig. 7a–c.

Further, Fig. 8 presents the tensile properties of the joints. The UTS/YS of joints C1, C, and F are 510/360, 500/349, and 391/345 MPa, respectively, while the elongation (EL) rate are 9.8, 4.5, and 5.7 %, respectively. These tensile test results
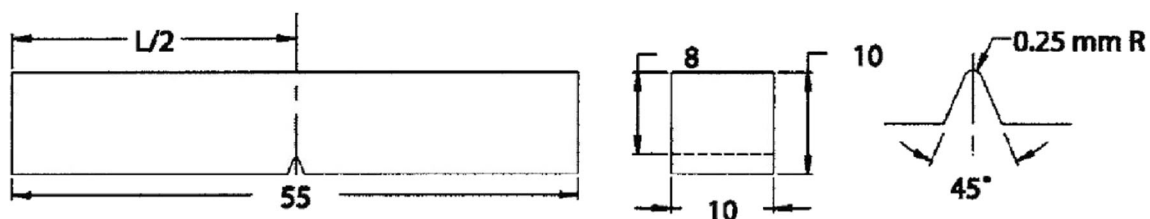

Fig. 3 Schematic diagram of the impact specimens

Fig. 4 **a** Different groove configuration shown schematically: *a1* joint type C1, *a2* joint type C, and *a3* joint type F (note that all dimensions are in mm). **b** Schematics showing the multiple weld pass sequences that were followed for completing the joints *b1* C1, *b2* C, and *b3* F. **c** Optical zoomed macrographs (at ×2) showing weld cross sections for the joints *c1* C1, *c2* C, and *c3* F, where the numbers *1*, *2*, and *3* represent the WM, HAZ, and BM, respectively
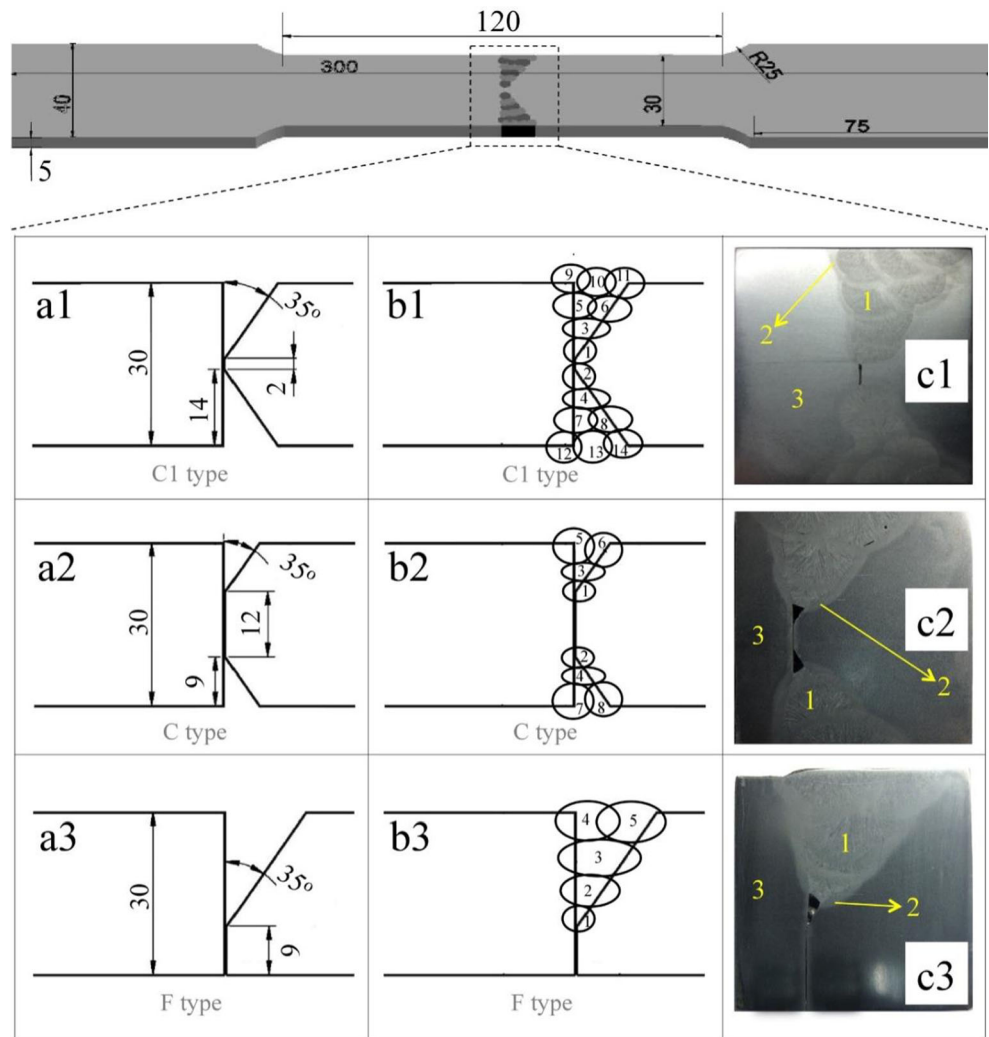
show that the C1 joint possessed the maximum YS and UTS while maintaining a ductility of 9.8 %, which could be attributed to the groove configuration and related defects such that cracks initiating in the HAZ of these joints, i.e., crack initiates almost at the center of the weld region in the C1 joint, whereas it initiates in the HAZ. Further, shear lip formation at their fractured surfaces is observed,

which indicates the predominant ductile fracture mode [11]. Furthermore, the difference in UTS/YS and ductility can be re-examined by the significantly different heat dissipation patterns, which resulted in a significant change in the YS of these joints.

The tensile specimens that were tested at room temperature, the associated fractured ends of the C1 joint,

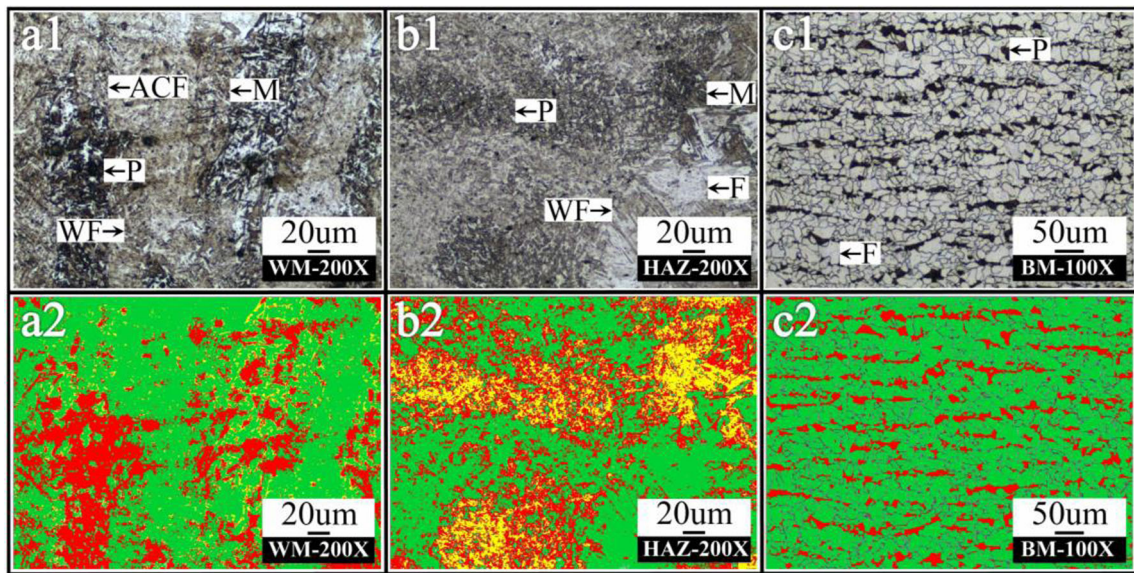**Fig. 5** OM microstructure of the WM, HAZ, and BM
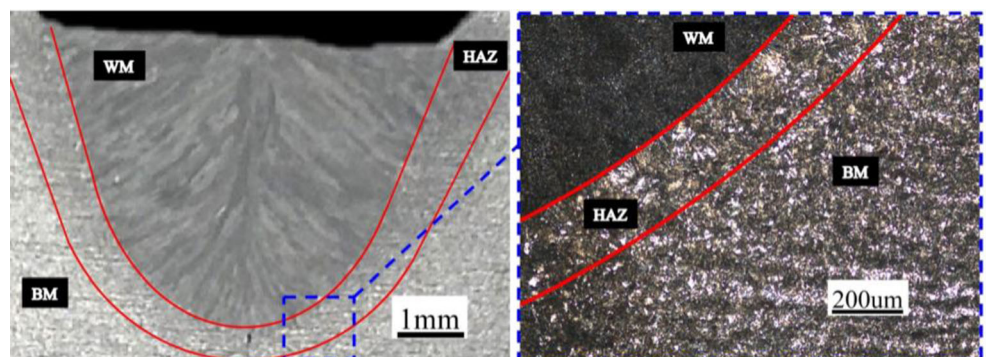
Fig. 6 OM microstructure and Image Pro Plus analysis of *a1–a2* the WM, *b1–b2* HAZ, and *c1-c2* BM

and the BM were selected for further SEM studies. As observed in the micrographs a3 and b3 shown in Fig. 9, both tearing topography surface (TTS) features in conjunction with a 45° dimpled rupture (DR) morphology can be discernible, indicating a mixed-mode fracture behavior. As previously reported, a very small scale microplastic tearing process could result in tearing topography. In the WM, another type of brittle transgranular fracture via cleavage along crystallographic planes can be clearly visible, presenting river patterns on top of the cleavage facets while the fracture initiation orients differently along the boundary of a grain.

3.2.2 Charpy impact properties

Room temperature Charpy impact testing was conducted on the V-notch specimens, and the results obtained are shown in Fig. 10. It is observed that the F joint possessed the maximum CVN value (162 J) out of all the joints, which is mainly attributed to the variation in weld sequences and the thermal gradients established. In particular, the refinement of the ACF and subsequently resultant primary phase of ferrite are found to be responsible for higher toughness, which coincides

well with a previous observation [27]. Furthermore, the impact properties of the WM increased proportionally with an increasing amount of ACF. Nevertheless, the decrease in toughness, despite a higher proportion of ACF, may be due to an overall coarse microstructure formed at a higher transformation temperature. In summary, our experimental results indicate that there is a decrease in toughness values of the weld metals due to the coarsened microstructure such as WF, which is in a good agreement with previously published data [24]. Furthermore, WF is usually undesirable in welds due to its poor toughness [28].

Figure 11 shows SEM micrographs of the Charpy impact tested specimens and the general ductile characteristics of failures in the fracture surface such as dense globular or elliptic dimples for the BM and C1 joint. From the SEM photos, the BM reveals coarser dimples compared with the C1 joint, which are in accordance with CVN energies, suggesting the existence of a significant amount of large dimples zones as well as small dimples zones as indicated in Fig. 11 a3. Furthermore, microvoid coalescence and the severe deformation characteristic of ductile fracture can be identified in the BM, which consistently correlates to a higher impact
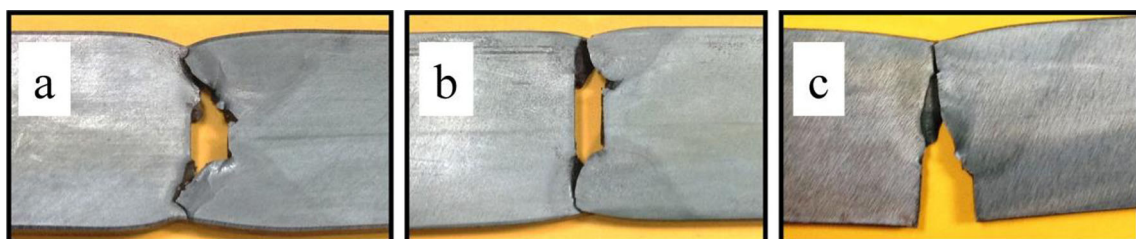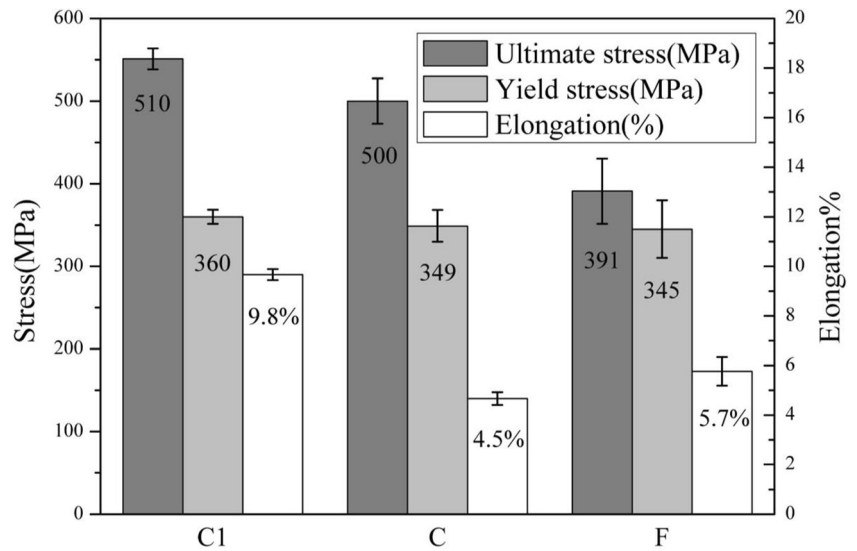

Fig. 7 Macrographs showing the location of fracture in the HAZ of the tensile tested specimens for joints **a** C1, **b** C, and **c** F

Fig. 8 Comparison of the mechanical properties for SS400 structural steel of the C1, C, and F weld grooves

toughness. On the other hand, Fig. 11 b1–b3 shows that the impact fracture surface of the C1 joint is predominantly characterized by transgranular cracks, particularly along grain boundaries of columnar

Fig. 9 SEM micrographs of the tensile tested specimens: *a1*, *a2*, and *a3* for the BM and *b1*, *b2*, and *b3* for the C1 joint
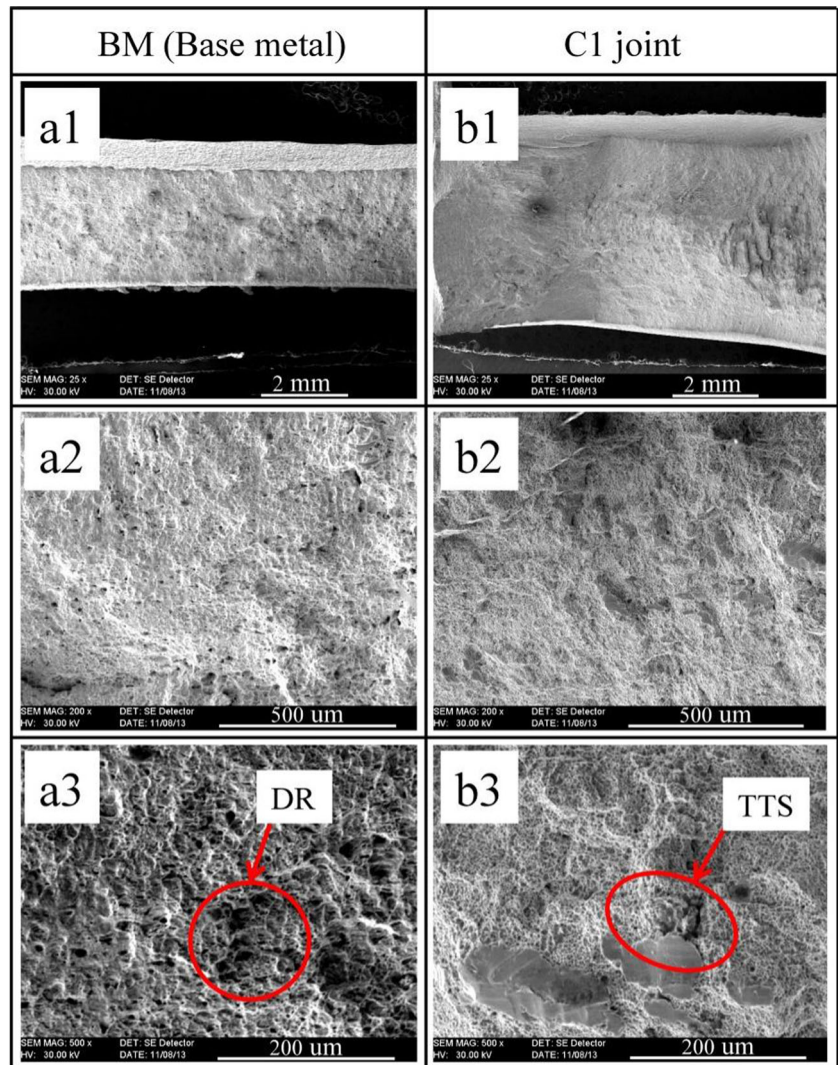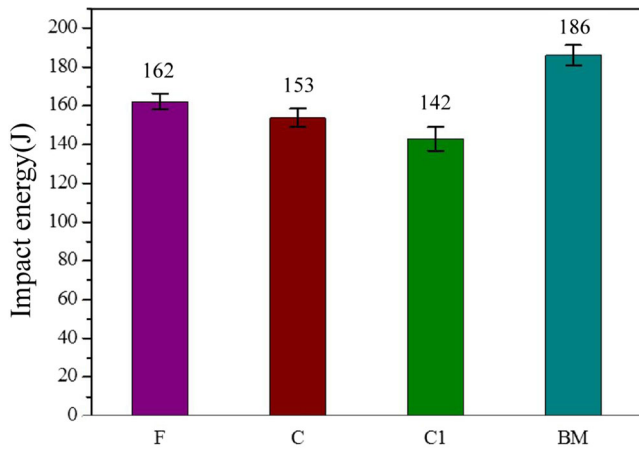
Fig. 10 Bar charts for SS400 structural steel with F, C1, and C joint types representing impact toughness (J)

dendritic structures, which translates to a lower impact toughness and a brittle fracture mode.

Fig. 11 SEM micrographs of the Charpy impact tested specimens: *a1*, *a2*, and *a3* for the BM at ×25, ×200, and ×500, respectively, and *b1*, *b2*, and *b3* for the C1 joint at ×25, ×200, and ×500,, respectively
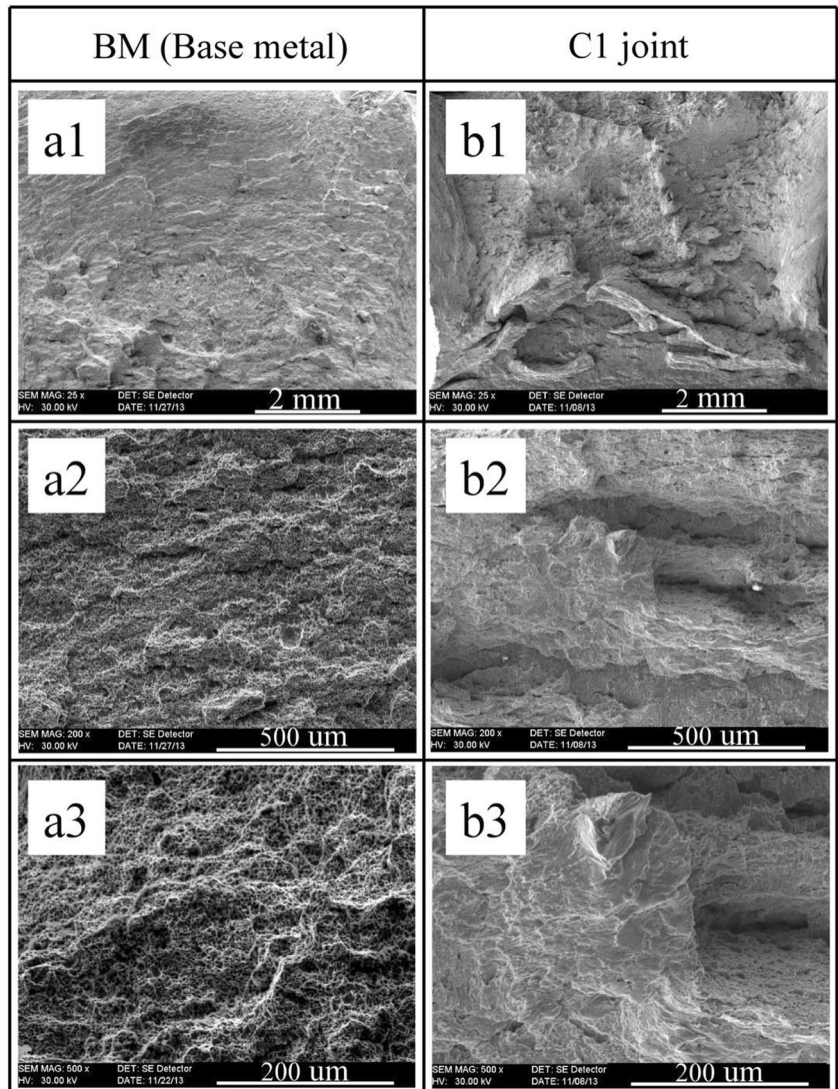
3.2.3 Microhardness

In order to evaluate microhardness variations across different locations of the joints, both vertical (designated as Y-axis values) and horizontal (designated as X-axis values) microhardness traverses down the center of the welds and different weld passes for different groove weld types were carried out. A relatively fine regular interval of 0.25 mm along the X/Y-axis was used to ensure sufficient resolutions for vertical and horizontal microhardness distributions for each type of joint as shown in Fig. 12. For the purpose of clear identification of the three distinctive WM, HAZ, and BM regions (designated as A, B, and C, respectively), the distribution curve of microhardness on the horizontal direction of the weld seam for F, C, and C1 joints was experimentally investigated. While traversing horizontally (X) across three different locations of these joints, a wide microhardness variation was observed in these zones, irrespective of F, C, and C1 joints. Another observation
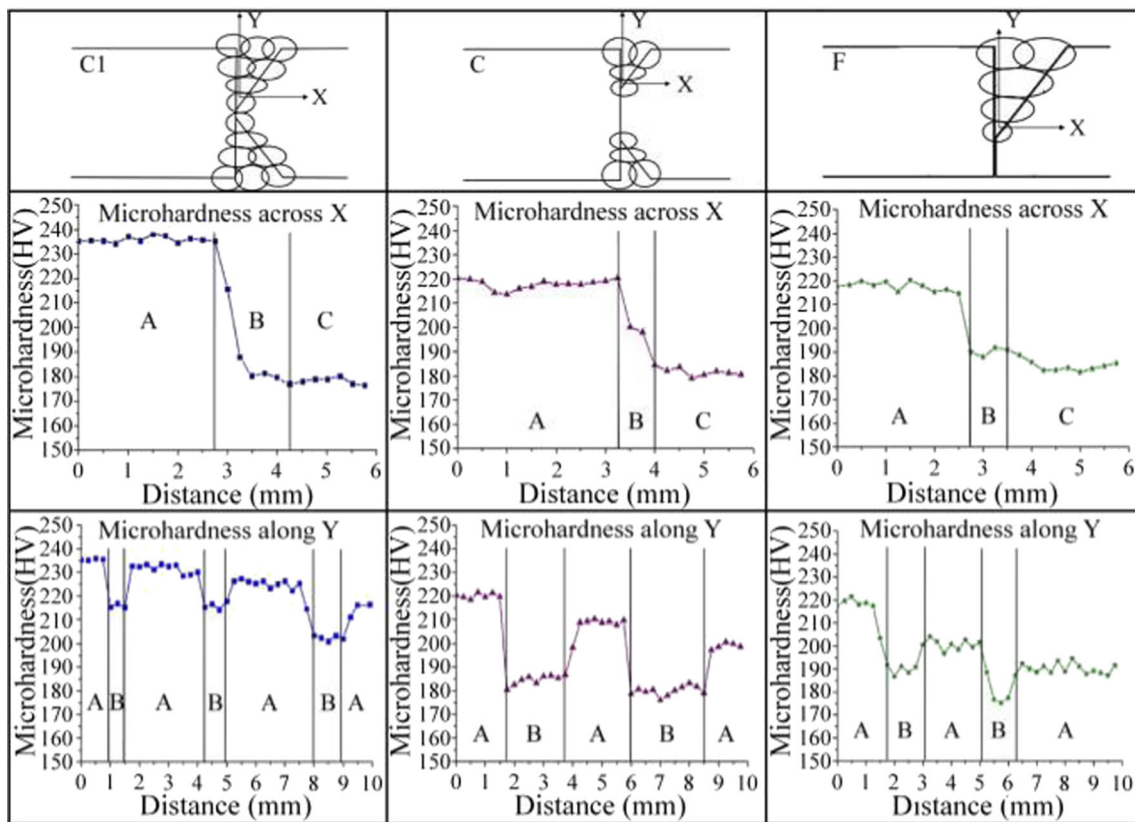
Fig. 12 Microhardness traverses across the weld vertically and horizontally, i.e., scan directions of X and Y to cover different weld passes and the BM for the C1, C, and F joints

was that while traversing from the bottom of the groove vertically upwards (Y), the microhardness was the highest at the bottom of the weld bead owing to a columnar microstructure. The columnar structure is induced by a higher cooling rate [29], and the highest microhardness was experimentally found to be closely related to columnar microstructure [30]. Then as a coarse grained microstructure gradually formed, the microhardness decreased. In a typical multi-pass welding process, the crystallographic structure of the first pass weld is primarily columnar grains. However, the subsequent passes with an additional heating effect will inevitably affect the microstructure afterwards such that an overlap region will transform the columnar grains into recrystallized coarse grained structures [30–32]. At the top of the weld bead, the microhardness value again increased due to the reheated areas of the WM and associated formation of a fine-grained region. Each weld bead experienced a similar trend, and Fig. 12 shows the microhardness results for 3–4 beads, which prevailed for the F, C, and C1 joints. The microhardness variation observed in the region of interest for all the joints is shown in the following texts: F(X-axis about 180~220HV)(Y-axis about 190~195HV), C(X-axis about 175~220HV)(Y-axis about 219~220HV), C1(X-axis about 155~235HV)(Y-axis about 215~218HV). In summary, the significant differences among similar zones of these

weldments can be experimentally measured to have drastically discernible microhardness values, which strongly suggests that groove configuration is an influentially important parameter in affecting the mechanical properties of these joints.

4 Conclusions

SS400 structural steel is ubiquitously used in the construction of engineering structures such as building frames due to the better overall performance in terms of strength, ductility, and welding performance. In this study, the crucial issues in the construction of precision press frame in terms of microstructure, microhardness, tensile properties, and impact toughness of JIS SS400 steel welded by a FCAW-G process were evaluated and compared, with particular focus on groove configuration.

The following conclusions can be drawn based upon the findings of this study:

1. In welding the thick sections of 40 mm JIS SS400 structural steel sheets, groove configuration and associated welding sequence was experimentally identified in this work as playing a significantly important role. The critical issue lies in controlling the weld heat dissipation

characteristics, owing to which the observed drastic change in the microstructure and mechanical properties of these welding joints.

2. Experimentation and the observation of microstructures showed that the welding sequence and groove weld types of a WM are the two most influential factors that need to be strongly controlled. In particular in the WM zone, predominantly consisting of ACF and small amount of martensite, the mechanical properties of tensile stress as well as elongation are strongly dependent on.

3. For the various groove configurations, the tensile test results demonstrated that the UTS/YS for joints C1, C, and F was 510/360, 500/349, and 391/345 MPa, respectively, while the EL was 9.8, 4.5, and 5.7 %, respectively. These tensile test results clearly showed that the C1 joint possessed the maximum YS and UTS while maintaining a relatively higher ductility of 9.8 %, which could be attributed to the groove configuration and related cracks initiated in the HAZ such that crack initiates almost at the C1 joint center of the weld region.

4. For the impact toughness, the F joint exhibits a relatively greater value of 162 J due to its comparatively high heat dissipation characteristics and the resulting fine ACF formation. Therefore, the impact properties of a WM increase proportionally with the amount of ACF. Nevertheless, the decrease in toughness, despite a higher proportion of ACF, may be due to an overall coarse microstructure formed at a higher transformation temperature.

5. The maximum value of microhardness occurs in the WM with a C1 joint, which is mainly attributed to the formation of martensite at a lower heat input as well as a faster cooling rate. In summary, the measured minimum and peak microhardness values demonstrate the significant differences among similar zones of these welded joints in various groove configurations, which strongly suggest that groove configuration is an important parameter in affecting the mechanical properties.

References

1. Murugan S, Rai SK, Kumar PV, Jayakumar T, Raj B, Bose MSC (2001) Temperature distribution and residual stresses due to multipass welding in type 304 stainless steel and low carbon steel weld pads. Int J Pres Ves Piping 78:307–317

2. Kang JG, Ryu GS, Kim DC, Kang MJ, Park YW, Rhee S (2013) Optimization of arc-start performance by wire-feeding control for GMA welding. J Mech Sci Technol 27(2):501–509

3. Kou S (2002) Welding metallurgy. 2nd ed. A Wiley-Interscience Publication

4. Babu SPK, Natarajan S (2010) High temperature corrosion and characterization studies in flux cored arc welded 2.25Cr-1Mo power plant steel. JMEPEG 19:743–750

5. Aloraier A, Almazrouee A, Shehata T, Price JWH (2012) Role of welding parameters using the flux cored arc welding process of low alloy steels on bead geometry and mechanical properties. JMEPEG 21:540–547

6. Quintino L, Liskevich O, Vilarinho L, Scotti A (2013) Heat input in full penetration welds in gas metal arc welding (GMAW). Int J Adv Manuf Technol 68:2833–2840

7. Liao MT, Chen WJ (1999) A comparison of gas metal arc welding with flux-cored wires and solid wires using shielding gas. Int J Adv Manuf Technol 15:49–53

8. Myers T (2010) Cost, overall operator appeal, and weld quality must all be considered when selecting the shielding gas for a flux cored arc welding application. Weld J 80:30–33

9. Kumar VV, Murugan N (2011) Effect of FCAW process parameters on weld bead geometry in stainless steel cladding. JMMCE 10:827–842

10. Moon HS, Kim YB, Beattie RJ (2006) Multi sensor data fusion for improving performance and reliability of fully automatic welding system. Int J Adv Manuf Technol 28:286–293

11. Sharma V, Shahi AS (2014) Effect of groove design on mechanical and metallurgical properties of quenched and tempered low alloy abrasion resistant steel welded joints. Mater Des 53:727–736

12. Aloraier AS, Ibrahim RN, Ghojel J (2004) Eliminating post-weld heat treatment in repair welding by temper bead technique: role bead sequence in metallurgical changes. J Mater Process Technol 153–154:392–400

13. Wang J, Li Y, Liu P (2003) Effect of weld heat input on toughness and structure of HAZ of a new super-high strength steel. Bull Mater Sci 26:301–305

14. Frydman S, Konat L, Pekalski G (2008) Structure and hardness changes in welded joints of Hardox steels. Arch Civil Mech Eng 8(4):15–27

15. Mirzaei M, Jeshvaghani RA, Yazdipour A, Zangeneh-Madar K (2013) Study of welding velocity and pulse frequency on microstructure and mechanical properties of pulsed gas metal arc welded high strength low alloy steel. Mater Des 51:709–713

16. Meric C, Tokdemir M (1999) An investigation of the weld region of the SAE 1020 joined with metal active gas and determination of the mismatch factor. JMEPEG 8:601–605

17. Gharibshahiyan E, Raouf AH, Parvin N, Rahimian M (2011) The effect of microstructure on hardness and toughness of low carbon welded steel using inert gas welding. Mater Des 32:2042–2048

18. Kumar S, Shahi AS (2011) Effect of heat input on the microstructure and mechanical properties of gas tungsten arc welded AISI 304 stainless steel joints. Mater Des 32:3617–3623

19. Lee JS, Jeong SH, Lim DY, Yun JO, Kim MH (2010) Effects of welding heat and travel speed on the impact property and microstructure of FC welds. Met Mater Int 16:827–832

20. Lan L, Qiu C, Zhao D, Gao X, Du L (2012) Analysis of martensite–austenite constituent and its effect on toughness in submerged arc welded joint of low carbon bainitic steel. J Mater Sci 47:4732–4742

21. Nascimentoa MP, Voorwalda HJC, Filho JCP (2011) Fatigue strength of tungsten inert gas-repaired weld joints in airplane critical structures. J Mater Process Technol 211:1126–1135

22. ASTM International (2013) Standard test methods for notched bar impact testing of metallic materials (ASTM E23-12c). ASTM International, West Conshohocken

23. ASTM International (2011) Standard test method for Knoop and Vickers hardness of materials (ASTM E384-11). ASTM International, West Conshohocken

24. Eroglu M, Aksoy M, Orhan N (1999) Effect of coarse initial grain size on microstructure and mechanical properties of weld metal and HAZ of a low carbon steel. Mater Sci Eng, A 269:59–66

25. Dyja D, Stradomski Z, Stachura S (2005) Solidification structure of massive castings from duplex cast steel. Arch Foundry 5:79–86

26. Loureiro AJR (2002) Effect of heat input on plastic deformation of undermatched welds. J Mater Process Technol 128:240–249

27. Diaz-Fuentes M, Iza-Mendia A, Gutierrez I (2003) Analysis of different acicular ferrite microstructures in low-carbon steels by electron backscattered diffraction. Study of their toughness behavior. Metall Mater Trans A 34A:2505–2516

28. Svensson LE (1994) Control of microstructures and properties in steel arc welding. CRC Press, Boca Raton, FL

29. Chen Y, Chen S, Li L (2008) Effects of heat input on microstructure and mechanical property of Al/Ti joints by rectangular spot laser welding-brazing method. Int J Adv Manuf Technol 44:265–272

30. Ramakrishnan M, Muthupandi V (2012) Application of submerged arc welding technology with cold wire addition for drum shell long seam butt welds of pressure vessel components. Int J Adv Manuf Technol 65:945–956

31. Hyde T, Sun W (2009) Creep damage modelling of welds with heterogeneous structures. 3rd International Conference on Integrity, Reliability and Failure, Porto/Portugal 20-24

32. Prasad K, Dwivedi DK (2006) Some investigations on microstructure and mechanical properties of submerged arc welded HSLA steel joints. Int J Adv Manuf Technol 36:475–483